



Novel $\text{ZnFe}_2\text{O}_4/\text{WO}_3$, a highly efficient visible-light photocatalytic system operated by a Z-scheme mechanism

Sher Bahadur Rawal¹, Hye Jin Kang¹, Dong-Il Won, Wan In Lee*

Department of Chemistry and Chemical Engineering, Inha University, Incheon 22212, Korea



ARTICLE INFO

Keywords:
Visible-light photocatalyst
heterojunction
 $\text{ZnFe}_2\text{O}_4/\text{WO}_3$
Z-scheme
oxidation reaction

ABSTRACT

Dark red ZnFe_2O_4 (ZFO) nanoparticles (NPs) of ~9 nm size and pale yellow WO_3 nanowire bundles (NWBs) with high porosity were prepared by hydrothermal reactions, respectively, and coupled to form novel ZFO/ WO_3 heterojunctions. Tiny ZFO NPs and highly porous WO_3 NWBs successfully formed intimate heterojunctions, facilitating charge transport at their interfaces. Under visible-light, ZFO/ WO_3 composites demonstrated outstanding catalytic activities for decomposing isopropyl alcohol (IPA) in the gas phase and salicylic acid (SA) in aqueous solution. In particular, the amount of CO_2 evolved in 2 h during decomposition of IPA was 24.7 ppmv, which was 3.0 times that produced using typical nitrogen-doped TiO_2 (N- TiO_2). Moreover, its degradation rate constant of SA in the presence of ZFO/ WO_3 was 7 times that of N- TiO_2 . It was determined that $\cdot\text{OH}$ and $\cdot\text{O}_2^-$ radicals were the major active species responsible for oxidation reactions, suggesting that the photocatalytic reactions of ZFO/ WO_3 occurred via Z-scheme mechanism.

1. Introduction

Use of visible-light as an energy source for photocatalytic reactions offers a potential strategy for removal of organic pollutants generated in our environments [1–3]. TiO_2 is considered the most efficient photocatalyst among various semiconductors [4–6], but its large bandgap ($E_g = 3.2$ eV) does not allow utilization of visible-light photons occupying ~45% of the solar spectrum [7–9].

Typically, narrowing the band gap of TiO_2 by doping with transition elements such as Fe, Cr, V and others [10–12] into the Ti site and/or anions such as C, N or S [13–15] into the O site is used to design visible-light photocatalysts. Heavy doping is required to achieve appreciable reductions in TiO_2 band gap in these systems, but increase of doping levels also causes marked increases in charge recombination rates. As a result, only a limited visible-light catalytic activity can be achieved in general. Recently, several narrow bandgap semiconductors (NBSs) such as BiVO_4 [16–18], Bi_2WO_6 [19], Ag_3PO_4 [20–22], Ag_2CrO_4 [23], $\text{Li}_9\text{Fe}_3(\text{P}_2\text{O}_7)_3(\text{PO}_4)_2$ [24], $\text{PbBi}_2\text{Nb}_2\text{O}_9$ [25], BiOBr [26], BiOI [26,27], and others have been reported to exhibit significant visible-light photocatalytic activities. However, the catalytic efficiencies of single-component NBSs are not high, due to unavoidable constraints in their energy band locations and high charge recombination rates caused by their intrinsically low charge mobility.

The limitations of single-component NBSs as visible-light

photocatalysts could be overcome by combining two NBSs with appropriate energy band positions. Those heterojunction systems can show visible-light catalytic properties via *p-n* junction or Z-scheme mechanisms, as determined by charge-flow pathways between two NBSs [28–30]. In *p-n* junction systems, photogenerated electrons in the CB of *p*-type NBS move to that of *n*-type NBS, and conversely holes in the VB of *n*-type NBS move to that of *p*-type NBS (see Fig. S1). As a result, photogenerated electrons and holes are spatially separated, thereby suppressing the electron-hole recombination. However, the reduced redox potentials of space-charge separated electrons and holes can degrade their chemical reactivity. Contrarily, Z-scheme systems offer the distinct advantage in achieving high reduction and oxidation potentials, but the electron transport from the CB of NBS2 to the VB of NBS1 in NBS1/NBS2 systems will be a critical step in determining their photocatalytic efficiencies (see Fig. S1).

In photocatalytic oxidation reactions, the major active species are $\cdot\text{OH}$ and $\cdot\text{O}_2^-$ radicals. As indicated in equations 1 and 2, +2.32 V (vs. NHE at pH 7) or more positive potential is required for efficient generation of $\cdot\text{OH}$, whereas -0.284 V (vs. NHE) or more negative potential is necessary for the generation of $\cdot\text{O}_2^-$. In principle, either $\cdot\text{OH}$ or $\cdot\text{O}_2^-$ can completely oxidize organic compounds, but both of them are required for high catalytic reactivity [31–33]. Hence, design of photocatalytic systems that can produce both of $\cdot\text{OH}$ and $\cdot\text{O}_2^-$ radicals under visible-light irradiation is required to develop efficient systems. From

* Corresponding author.

E-mail address: wanin@inha.ac.kr (W.I. Lee).

¹ These authors contributed equally.

this point of view, Z-scheme-based catalysts are considered to be a highly promising system.



Various Z-scheme systems have been extensively investigated over the last few decades. For instance, CuBi₂O₄/WO₃ [34], NaNbO₃/WO₃ [35], CaFe₂O₄/WO₃ [36], PbBi₂Nb_{1.9}Ti_{0.1}O₉/WO₃ [37], g-C₃N₄/WO₃ [38,39], AgX (X = Br, I)/Ag₃PO₄ [40,41], g-C₃N₄/BiVO₄ [42], g-C₃N₄/Ag₃PO₄ [43], g-C₃N₄/MoS₂ [44], g-C₃N₄/FeWO₄ [45], MoS₂/Bi₂MoO₆ [46], AgBr/BiVO₄ [47] and others have been reported to show meaningful catalytic efficiencies for the decompositions of organic pollutants under visible-light. However, outstanding catalytic systems eligible for commercial application have not been developed yet. Presumably, Z-scheme-based charge transport between two NBSs represents a bottleneck, which implies more systematic investigation and diverse attempts have to be performed to identify NBS pairs capable of providing efficient charge transport and high catalytic performance.

In the present study, for the first time, we combined ZnFe₂O₄ (ZFO) and WO₃ with a view to design an efficient Z-scheme photocatalytic system working under visible-light, as shown in Fig. 1. WO₃ has frequently been utilized as a component of Z-scheme systems due to its highly positive VB level (+2.73 V vs. NHE at pH 7), which is an appropriate potential for oxidizing H₂O and OH⁻ to ·OH [34–39]. On the other hand, ZFO with a band gap of 1.87 eV shows excellent visible-light absorption characteristics, and its CB level of -0.39 V vs. NHE at pH 7 is eligible for reducing molecular oxygen to ·O₂⁻ radical. Bare ZFO shows a poor photocatalytic activity due to the rapid charge recombination [48], but it is expected to be a promising sensitizer for formation of heterojunction-based photocatalysts although only a few systems have been reported to date [49–52]. Moreover, highly dispersible 9 nm-sized ZFO NPs are suitable for producing excellent contact onto the highly porous WO₃ NWB. Visible-light photocatalytic properties for the fabricated ZFO/WO₃ systems with various compositions were analyzed by monitoring the decomposition of gaseous isopropyl alcohol (IPA) and aqueous salicylic acid (SA). In addition, we systematically investigated the photocatalytic mechanism involved and discussed the reasons why ZFO/WO₃ systems had such outstanding photocatalytic activities.

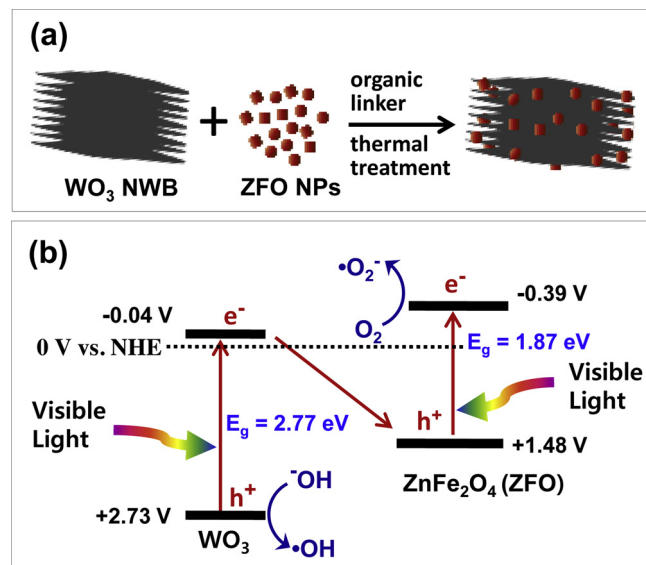


Fig. 1. Synthetic strategy of ZFO/WO₃ heterojunction structures (a) and energy band diagram of ZFO/WO₃ describing the charge flow and photocatalytic mechanism under visible-light irradiation (b). All potentials were indicated vs. NHE at pH 7.

2. Experimental Section

2.1. Preparation of ZFO, WO₃ and ZFO/WO₃ composites

ZnFe₂O₄ (ZFO) NPs were synthesized by modifying a hydrothermal process reported previously [53]. In a typical procedure, 2.5 mmol Zn (NO₃)₂·6H₂O was mixed with 5 mmol Fe(NO₃)₃·9H₂O in 40 mL distilled water, and the pH of the mixture was adjusted to 13 by adding 6 M KOH solution with vigorous stirring. The reaction mixture was then placed in a Teflon-lined autoclave and allowed to react for 8 h at 190 °C. After the reaction, the obtained slurry was filtered, washed several times with distilled water, and dried in a vacuum oven at 100 °C.

To synthesize WO₃ nanowire bundles (NWBs), 3.0 mmol of WCl₄ was dissolved in 50 mL isopropyl alcohol with vigorous stirring for 2 h. The reaction mixture was then transferred to a Teflon-lined autoclave for a solvothermal reaction at 160 °C for 30 h. The precipitate formed was then collected, washed several times with ethanol, and dried in a vacuum oven at 100 °C. As-prepared NWBs were dark blue in color indicative of W₁₈O₄₉ phase, and were then converted to WO₃ NWBs by post-annealing at 430 °C for 3 h in air.

To produce ZFO/WO₃ heterojunction structures (see Fig. 1a), 0.30 g of WO₃ NWBs were suspended in 30 ml ethanol and then 0.5 g maleic acid was added. After stirring for 2 h, stoichiometric amounts of ZFO NPs were added to this suspension to prepare ZFO/WO₃ composites with different compositions. Typically, to prepare the 10/90 ZFO/WO₃ composite, which contains ZFO and WO₃ in a 1:9 ratio by weight, 0.033 g ZFO NP was added to the WO₃ NWB suspension and stirred for 12 h at 60 °C. The prepared ZFO/WO₃ powders were collected by centrifugation, washed by distilled water several times, dried under vacuum at 100 °C, and then heat-treated at 300 °C for 3 h to remove organics.

2.2. Characterization

Powder X-ray diffraction (XRD) patterns were obtained using a Rigaku Multiflex diffractometer with monochromatic Cu K α radiation ($\lambda = 1.5406 \text{ \AA}$). UV-visible diffuse reflectance spectra were acquired using a Perkin-Elmer Lambda 40 spectrophotometer with applying BaSO₄ as the reflectance standard. Transmission electron microscope (TEM) images were obtained by a JOEL JEM 2100 F operated at 200 kV. For TEM analysis, 1 mg of each sample was dispersed in 50 mL of ethanol and a single drop of this suspension was then spread on a holey amorphous carbon coated Ni grid (JEOL Ltd.) [54].

The flat-band potential (V_{fb}) of ZFO and WO₃ were determined by Mott-Schottky method [55,56]. The ZFO NPs and WO₃ NWBs were deposited on a $1 \times 1 \text{ cm}^2$ Pt-coated Pyrex glass. A Pt wire and Ag/AgCl/0.1 M KCl electrode were used as counter and reference electrodes, respectively, while 0.2 M LiClO₄ in acetonitrile was used as electrolyte (pH 3.8). Electrochemical workstation (CHI660B, CH Instrument) was used to obtain the Mott-Schottky plots, and the potentiostatic impedance measurements were performed in the range of -0.5 to +1.0 V in 10 Hz.

2.3. Evaluation of visible-light photocatalytic activities

First, the photocatalytic activities of various catalytic samples were evaluated by monitoring the decomposition of IPA in the gas phase. Briefly, an aqueous suspension containing 8.0 mg of each photocatalyst was spread on a $2.5 \times 2.5 \text{ cm}^2$ Pyrex glass and dried. The gas reactor system used to evaluate photocatalytic activities was described elsewhere [54]. Visible-light was produced by passing the light emitted from a 300 W Xe lamp (Oriol) through a UV cut-off filter ($\leq 422 \text{ nm}$, ZUL0422 ASAHI Co.) and a water filter. After evacuating the reactor, 1.6 μL of an aqueous solution of IPA (IPA:H₂O = 1:9 by volume) was injected. The initial concentration of gaseous IPA in the reactor was 117 ppm by volume (ppmv). Reactor pressure was controlled at

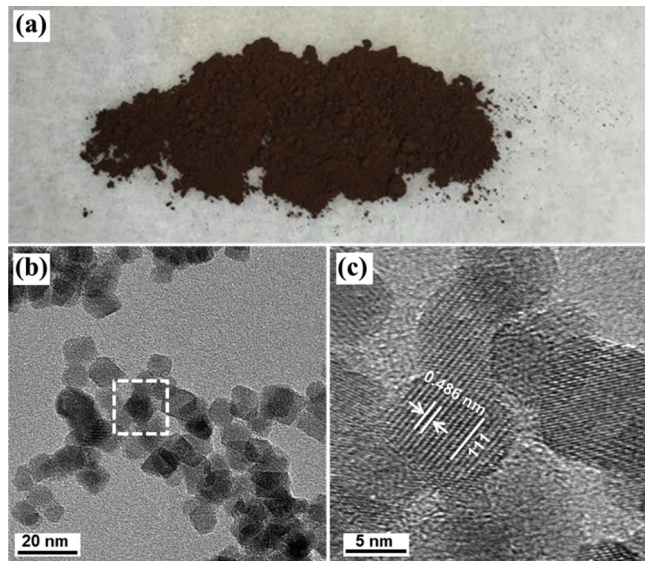


Fig. 2. Photographic image (a) and TEM images (b, c) of as-prepared ZFO NPs. c is the magnified image of the dotted square part in b.

750 Torr by adding oxygen. After every 30 min of irradiation, 0.5 mL of the gas sample was forwarded to a gas chromatograph (Agilent Technologies, Model 6890 N) using an auto sampling valve system. A methanizer was installed between the GC column outlet and the FID detector to detect CO_2 .

Second, the photocatalytic activities of samples were assessed by monitoring the decomposition of salicylic acid (SA) in aqueous solution. Briefly, 10 mg of catalytic samples were suspended in 50 mL of 50 μM aqueous SA solution with magnetic stirring in the dark. SA concentration was measured after every 30 min of visible-light irradiation by monitoring its characteristic absorption peak at 295 nm using a UV-visible spectrophotometer (Perkin-Elmer Lambda 40).

3. Results and discussion

Hydrothermally synthesized ZFO NPs were dark red in color, as shown in Fig. 2a. TEM image in Fig. 2b shows that as-prepared ZFO NPs are monodispersed with an average size of ~ 9 nm, and look mutually separated without significant agglomeration. A magnified TEM image in Fig. 2c exhibits uniform fringe patterns over a whole particle, which suggests individual ZFO NPs are single crystals. The inter-plane distance of 0.486 nm estimated from the fringe patterns corresponds to the d_{111} of the cubic ZFO phase.

TEM image in Fig. 3a shows $\text{W}_{18}\text{O}_{49}$ NWBs, as-prepared by solvothermal reaction at 160 $^{\circ}\text{C}$. The $\text{W}_{18}\text{O}_{49}$ NWBs were composed of assemblies of individual $\text{W}_{18}\text{O}_{49}$ nanowires (NWs). Fig. 3b shows a magnified TEM image of the individual NWs in the dotted square part of Fig. 3a. The uniform fringe patterns observed with a spacing of 0.378 nm correspond to the (010) plane of the monoclinic $\text{W}_{18}\text{O}_{49}$ phase, which suggests individual NWs grew in the direction of the (010) plane. These $\text{W}_{18}\text{O}_{49}$ NWBs were converted to WO_3 NWBs by thermal treatment at 430 $^{\circ}\text{C}$ in air. Noticeably, as shown in Fig. 3c, prepared WO_3 NWBs have the same shape as $\text{W}_{18}\text{O}_{49}$ NWBs, indicating that oxygen deficient $\text{W}_{18}\text{O}_{49}$ is oxidized to WO_3 phase without changing its initial morphology. The uniform fringe patterns with an inter-plane spacing of 0.377 nm, as shown in the magnified TEM image of WO_3 NWB in Fig. 3d, is considered to represent the (020) plane of monoclinic WO_3 phase, indicating the direction of crystallographic plane was not altered during the phase transformation from $\text{W}_{18}\text{O}_{49}$ to WO_3 . The BET surface areas of $\text{W}_{18}\text{O}_{49}$ and WO_3 NWB were $53 \text{ m}^2 \text{ g}^{-1}$ and $27 \text{ m}^2 \text{ g}^{-1}$, respectively. Although the surface area was reduced by about 50% by thermal treatment, the prepared WO_3 NWBs are still highly porous and have

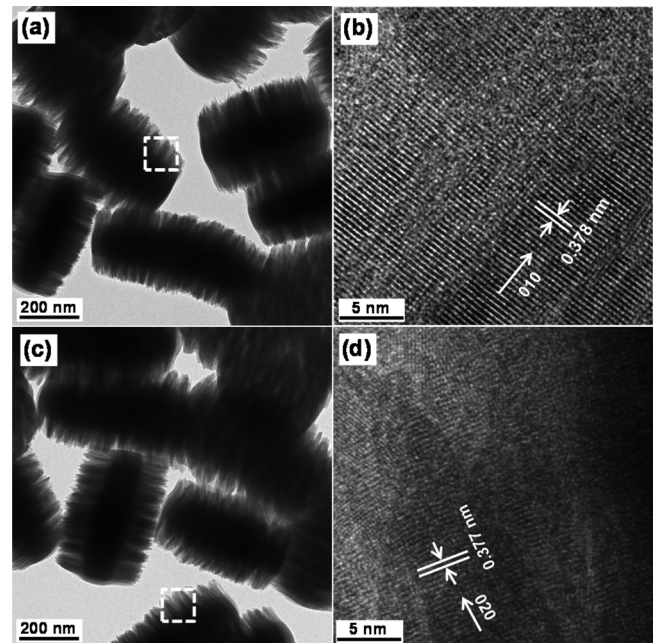


Fig. 3. TEM image of $\text{W}_{18}\text{O}_{49}$ NWBs as-prepared by solvothermal reaction (a) and its magnified image (b). TEM image of WO_3 NWBs obtained by post thermal treatment (c) and its magnified image (d).

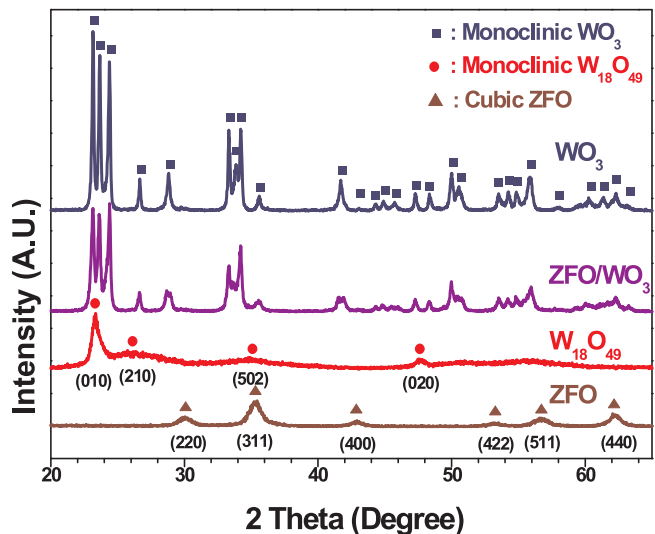
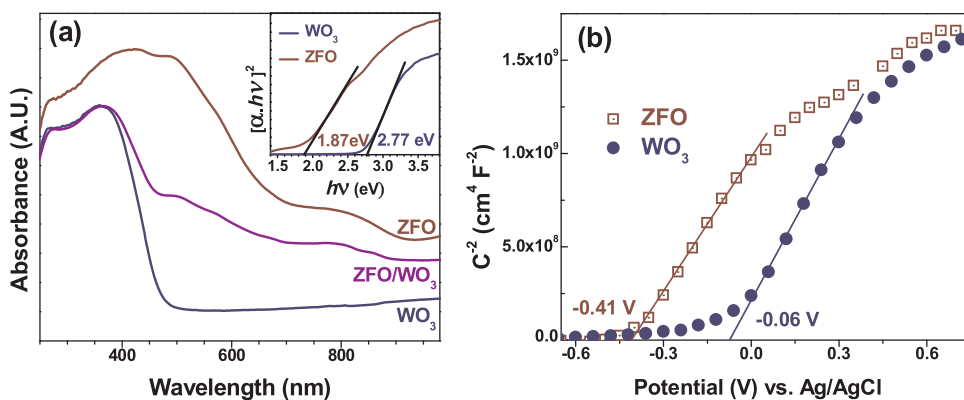


Fig. 4. XRD patterns of ZFO NPs, $\text{W}_{18}\text{O}_{49}$ and WO_3 NWBs, and 10/90 ZFO/ WO_3 composites.

large surface area.

The XRD patterns of ZFO NPs in Fig. 4 exhibited diffraction peaks at 29.94 $^{\circ}$, 35.27 $^{\circ}$, 42.86 $^{\circ}$, 53.16 $^{\circ}$, 56.67 $^{\circ}$, and 62.22 $^{\circ}$, which correspond to the (220), (311), (400), (422), (511) and (440) planes of the spinel ZFO phase (JCPDS, No. 65-3111). Average crystallite size calculated from the (311) peak using the Scherrer equation was determined to be 8.9 nm, which matches the particle size observed from the TEM image. XRD patterns of $\text{W}_{18}\text{O}_{49}$ NWBs, as-prepared by solvothermal reaction (Fig. 4), exhibits diffraction peaks at 23.52 $^{\circ}$, 25.88 $^{\circ}$, 35.57 $^{\circ}$, and 48.16 $^{\circ}$, which correspond to the (010), (210), (502) and (020) planes of the monoclinic $\text{W}_{18}\text{O}_{49}$ phase (JCPDS, No. 05-0392). X-ray diffraction patterns of the WO_3 NWBs (Fig. 4), obtained by oxidation of $\text{W}_{18}\text{O}_{49}$ NWBs at 430 $^{\circ}\text{C}$, also correspond to the monoclinic WO_3 phase (JCPDS, No. 83-0950), indicating that $\text{W}_{18}\text{O}_{49}$ was completely converted to the WO_3 phase.



UV-visible diffuse reflectance spectra obtained in absorption mode show that ZFO NPs exhibit a strong absorption in the visible range with an absorption edge of ~700 nm, as shown in Fig. 5a. The optical band gap (E_g) of as-prepared ZFO NPs was determined using the Kubelka-Munk equation,

$$[\alpha h\nu]^{1/p} = A(h\nu - E_g) \quad (3)$$

where α is the optical absorption coefficient, $h\nu$ is photonic energy, A is a proportionality constant, and p is 1/2 for direct transition, whereas p is 2 for indirect transition. By setting $p = 1/2$, the direct bandgap of ZFO NPs was determined by the plotting $[\alpha h\nu]^2$ vs. $h\nu$, as shown in the inset of Fig. 5a. E_g of ZFO NPs was determined to be 1.87 eV, and using the same method, the E_g of WO_3 NWBs was determined to be 2.77 eV.

Flat-band potentials of ZFO NPs and WO_3 NWBs were determined using the Mott-Schottky method [55,56]. From the Mott-Schottky plots shown in Fig. 5b, the onset potentials of ZFO NPs and WO_3 NWBs were estimated to be -0.41 V and -0.06 V, respectively, vs. Ag/AgCl at pH 3.8, which are converted to -0.39 V and -0.04 V, respectively, vs. NHE at pH 7. The determined flat-band potential of ZFO NPs is compatible with the reported values in the literature [57–59]. As a result, the VB levels of ZFO NPs and WO_3 NWBs were determined to be +1.48 V and +2.73 V vs. NHE, respectively, as shown in the energy band of ZFO/ WO_3 in Fig. 1b. Thus, effective electron transport from the CB of WO_3 to the VB of ZFO is expected for the ZFO/ WO_3 heterostructures when exposed to visible-light, as the VB of ZFO NPs (+1.48 V vs. NHE) is located in the middle of the CB (-0.04 V vs. NHE) and VB (+2.73 V vs. NHE) of WO_3 NWBs.

To produce ZFO/ WO_3 composites, ZFO NPs were combined with highly porous WO_3 NWBs using maleic acid as a linker, as described in Fig. 1a. The X-ray diffraction patterns of 10/90 ZFO/ WO_3 (ZFO: WO_3 = 10:90 in wt% ratio), as shown in Fig. 4, exhibits mixed diffraction patterns of cubic ZFO and monoclinic WO_3 phases without any impurity peaks, suggesting no appreciable chemical reaction between ZFO and WO_3 during heat-treatment at 300 °C. The UV-visible diffuse reflectance spectrum of the 10/90 ZFO/ WO_3 composite (Fig. 5a) reveals that the absorption edge is significantly shifted to longer wavelength comparing with that of bare WO_3 and that the total amounts of visible-light absorption by ZFO and WO_3 in the 10/90 ZFO/ WO_3 are approximately equal, because ZFO absorbs visible-light much more strongly than WO_3 . TEM images of the 10/90 ZFO/ WO_3 composite are shown in Fig. 6. TEM image of the ZFO and WO_3 interface in Fig. 6b indicates ~9 nm-sized ZFO NPs are intimately bound to the surfaces of WO_3 NWBs. The image in the inset in Fig. 6b shows that individual ZFO NPs are also deposited on the internal surfaces of WO_3 NWBs.

Photocatalytic activities of ZFO, WO_3 and ZFO/ WO_3 composites under an illumination of visible-light ($\lambda \geq 422$ nm) were evaluated with respect to the decomposition of gaseous IPA. As shown in Fig. 7a, IPA decomposition percentages by WO_3 NWBs and ZFO NPs were ~60% and ~8%, respectively, in 2 h. On the other hand, ZFO/ WO_3 showed much higher catalytic activities, and the 10/90 ZFO/ WO_3 composite

Fig. 5. UV-visible diffuse reflectance spectra of ZFO NPs, WO_3 NWBs and 10/90 ZFO/ WO_3 (a), and Mott-Schottky plots of ZFO NPs and WO_3 NWBs (b). Active area was 1 cm², and the electrolyte system (0.2 M LiClO₄ in acetonitrile at pH 3.8) was placed in a three-electrode cell, consisting of photoanode working electrode, Pt wire counter electrode, and saturated Ag/AgCl reference electrode.

demonstrated highest photocatalytic activity: IPA was completely removed in 90–120 min of irradiation. When the ZFO component increased beyond 10 wt %, the photocatalytic activity of the composite gradually decreased.

Photocatalytic activity was also evaluated by monitoring CO₂ evolution. As shown in Fig. 7b, the 10/90 ZFO/ WO_3 composite also exhibit highest activity: bare WO_3 NWBs and ZFO NPs produced only 4.5 and 3.1 ppmv CO₂ in 2 h, whereas its coupled system produces 24.7 ppmv of CO₂ in 2 h, which is remarkably higher amount comparing with 8.2 ppmv in 2 h by a typical N-doped TiO₂ [33,60].

Photocatalytic reaction with 10/90 ZFO/ WO_3 has been monitored for a long time until IPA is completely mineralized. It was reported that IPA is initially converted to acetone, and then gradually mineralized to form CO₂ and H₂O [61,62]. In our experiment, initial concentration of gaseous IPA in the reactor was 117 ppmv, suggesting that ultimate concentration of CO₂ is 351 ppmv. As shown in Fig. 7c, IPA was completely removed in 2 h visible-light irradiation, and the concentration of acetone was maximized at this time. Then acetone level was slowly decreased and totally disappeared in about 18 h. In 22 h, the concentration of CO₂ evolved reached approximately 350 ppmv without further increase in its level. Obtained result clearly shows that disappearance of a model compound does not indicate its complete decomposition, but suggests a passage of initial step in a lengthy decomposition pathway. Indeed, we observed that much longer time was required for the complete mineralization, but the ZFO/ WO_3 systems developed in this work could completely mineralize IPA under visible-light irradiation. Thus we believe that monitoring of CO₂ evolution provides meaningful and reliable data in evaluating the photocatalytic activity.

In addition, the photocatalytic activity of ZFO/ WO_3 was evaluated by monitoring salicylic acid (SA) degradation in aqueous solution. SA concentrations were determined by measuring its characteristic absorption at 296 nm. In aqueous solution, the photocatalytic decomposition of SA follows first order kinetics. That is, the photocatalytic reaction with elapse of time (t) can be simply described as $-d[c]/dt = k_r[c]$, where $[c]$ is the concentration of SA, and k_r denotes the overall degradation rate constant. In the present study, we defined k_r value as photocatalytic activity of each sample. As shown in Fig. 7d, 10/90 ZFO/ WO_3 had the highest catalytic activity, and the pattern of activities as a function of relative composition was quite similar to that of IPA decomposition in the gas phase. Notably, the degradation rate constant of 10/90 ZFO/ WO_3 was > 120 times that of ZFO, ~11 times that of WO_3 and ~7 times that of N-TiO₂.

A putative Z-scheme mechanism for photocatalysis by ZFO/ WO_3 heterojunction system is described in Fig. 1b. Briefly, when irradiated with visible-light, electrons in the VBs of WO_3 and ZFO are excited to their corresponding CBs, and then electrons in the CB of WO_3 (-0.04 V vs. NHE) transfer to the VB of ZFO (+1.48 V vs. NHE), which leaves holes in the VB of WO_3 and electrons in the CB of ZFO. These electrons and holes have elongated lifetimes due to space-charge separation, and

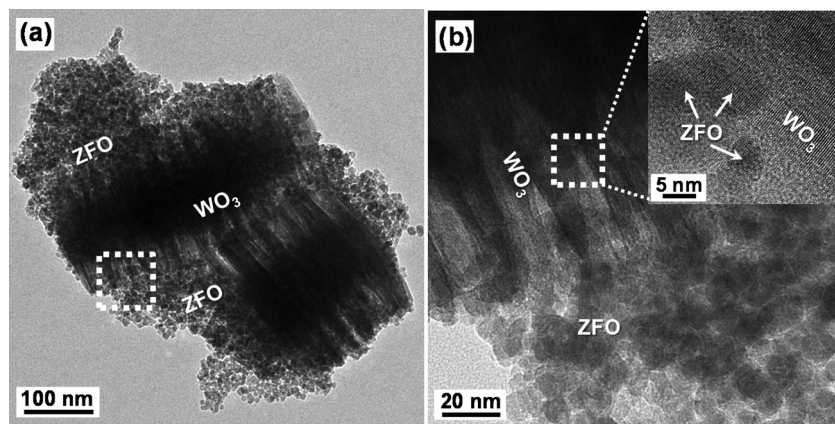


Fig. 6. TEM images of 10/90 ZFO/WO₃ composites. b is the magnified image of the dotted square part in a, and further magnified image is shown in the inset of b.

have strong reductive and oxidative powers, respectively. More specifically, holes in the VB of WO₃ with an energy level of +2.73 V vs. NHE can effectively produce •OH radicals by reacting with OH⁻ or H₂O, and the electrons in the CB of ZFO with an energy level of -0.39 V vs. NHE possess an enough reducing power to generate •O₂⁻ by reacting with O₂ and subsequently forming HO₂[•] by reacting with a proton (O₂ + H⁺ + e⁻ → HO₂[•], E₀ = -0.046 V vs. NHE). It is well-known that •OH is the principal oxidative species involved in the decomposition of organic pollutants and that the additional presence of •O₂⁻ or HO₂[•] further enhances oxidation reactions [31–33]. Therefore, we suggest that the remarkably high photocatalytic activity of the ZFO/WO₃ system is primarily due to the generations of •OH and •O₂⁻ simultaneously under visible-light irradiation.

An important requirement for efficient Z-scheme photocatalysts would be generating equal amount of electron/hole pairs for the two NBSs during visible-light irradiation. Then, the charge recombination occurring at each NBS can be minimized, and the irradiated photons will be utilized more effectively. This can be achieved by adjusting the compositional ratio of individual NBSs in forming the heterojunction, although their light absorption coefficient and spectral range of

absorption are different. As shown in Fig. 5a, ZFO absorbs approximately 10 times more photons than WO₃ in the range of 400–700 nm. Thus, to balance the total visible-light absorption, the quantity of ZFO employed to ZFO/WO₃ has to be 1/10 that of WO₃, which could explain why the 10/90 ZFO/WO₃ composite provides optimum photocatalytic activity.

To obtain evidence for this Z-scheme mechanism, we performed several experiments. First, we monitored •O₂⁻ radical concentrations during photocatalytic reactions under visible-light irradiation, using luminol (5-amino-2,3-dihydro-1,4-phthalazinedione) as a chemiluminescent (CL) probe for •O₂⁻ radical [63–65]. It is well known that the •O₂⁻ radical readily reacts with luminol in basic solution to generate 3-amino phthalate (AP) [63], which emits the characteristic fluorescence peak at 420 nm. As shown in Fig. 8a, no appreciable fluorescence peak was observed when bare WO₃ NWB were exposed to visible-light ($\lambda \geq 422$ nm), indicating the reduction potential of electrons generated in the CB of WO₃ is insufficient to convert O₂ to •O₂⁻. Similarly, bare ZFO NPs did not induce significant fluorescence peaks, although their CB potential is sufficiently negative to reduce O₂. This result suggests that the excited electrons of the bare ZFO cannot be utilized for O₂

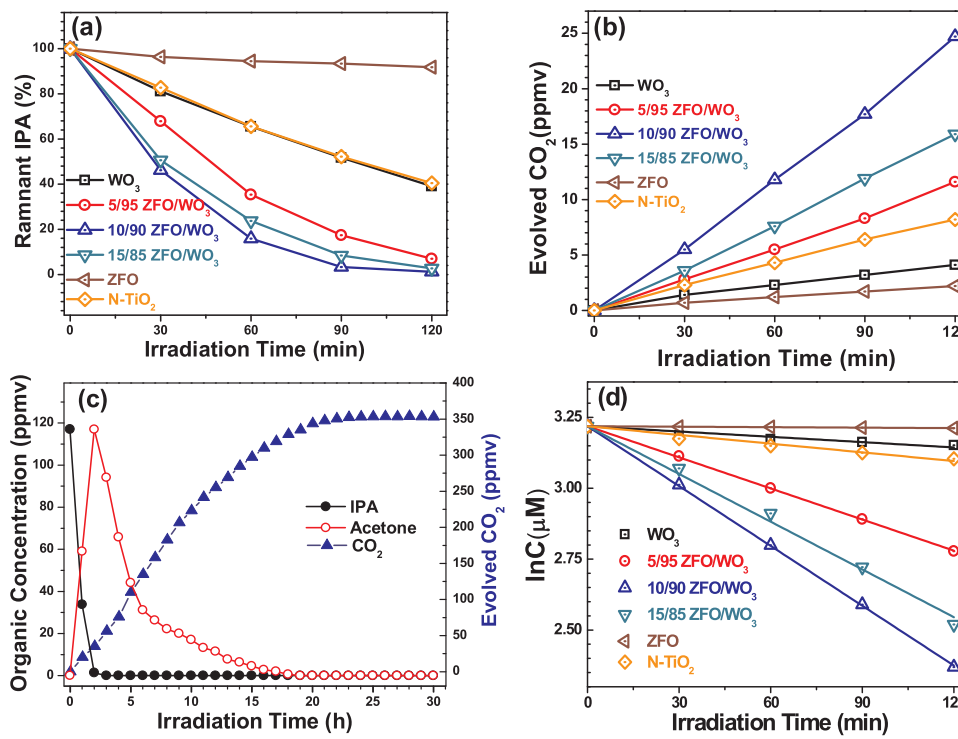


Fig. 7. Photocatalytic removal of gaseous IPA (a) and evolution of CO₂ (b) as a function of irradiation time with various catalytic systems. (c) Complete mineralization of IPA with 10/90 ZFO/WO₃ by long-term irradiation. (d) Remnant SA concentration as a function of irradiation time in the decomposition reaction of aqueous SA. In all experiments, $\lambda \geq 422$ nm light from 300 W Xe lamp was used as visible-light source.

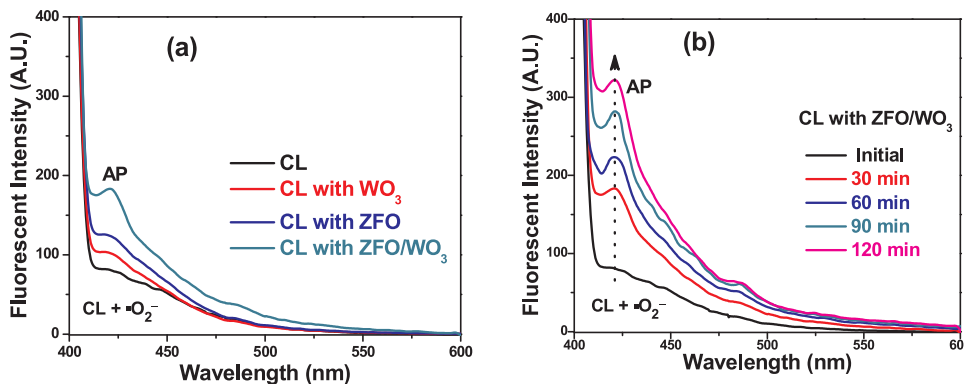


Fig. 8. Fluorescence spectra monitored after 30 min of visible-light ($\lambda \geq 422 \text{ nm}$) irradiation for the aqueous suspensions containing luminol and various catalytic samples (a) and the intensity change of AP as a function of irradiation time for the suspension with 10/90 ZFO/ WO_3 composite. In a typical reaction, 20 mg catalytic sample was suspended in 50 mL of 1.58 mM luminol aqueous solution containing 0.01 M NaOH. The excitation wavelength was 387 nm.

reduction due to rapid electron-hole recombination. In contrast, when 10/90 ZFO/ WO_3 system was employed, a strong emission peak at 420 nm, identified as the characteristic fluorescence peak of AP, was observed, and its intensity increased with irradiation time, as shown in Fig. 8b. This result indicates that O_2^- radicals are produced on the surface of ZFO/ WO_3 and that the catalytic reaction is dominated by a Z-scheme mechanism and not by a *p-n* junction mechanism.

Second, the effects of several scavengers for the photocatalytic reaction in aqueous phase were analyzed. Ammonium oxalate (AO), benzoquinone (BQ) and IPA are well-known scavengers of h^+ , O_2^- , and OH , respectively [31,66,67]. Herein we added these scavengers during the removal reaction of SA under visible-light to determine the major oxidizing species generated in the ZFO/ WO_3 systems. As shown in Fig. S2, the photocatalytic activities of 10/90 ZFO/ WO_3 were considerably decreased by adding BQ or IPA, but were not significantly changed by the addition of AO. Hence, O_2^- , and OH turns out to be the main species participating in decomposition of SA, which agrees with the result of CL probe experiment.

Third, we introduced Au NPs at the interface of ZFO and WO_3 and monitored the modification of photocatalytic activity. For Z-scheme photocatalysts, it has been known that charge flow between two NBSs can be expedited by introducing noble metals at their interfaces, resultantly leading to increase of photocatalytic activities [37,41,68,69]. Herein, Au NPs were introduced between ZFO NP and WO_3 NWB using mercaptopropionic acid as organic linker. TEM images for the fabricated photocatalytic system (10/90 ZFO/Au/ WO_3) and its charge flow diagram during visible-light irradiation are illustrated in Fig. 9. Due to an appropriate location of Au Fermi level, which is defined from its work function (5.1 eV or +0.6 V vs. NHE), the interfacial Au is expected to promote electron transport from the CB of WO_3 to the VB of ZFO. As seen in Fig. 10, 10/90 ZFO/Au/ WO_3 produces ~1.6 times of CO_2 in 2 h comparing with bare 10/90 ZFO/ WO_3 . The obtained result strongly supports that photocatalytic mechanism occurring on ZFO/Au/ WO_3 system is mainly based on Z-scheme process.

Photocatalytic activities of ZFO/ WO_3 were compared with that of a simple mixture of ZFO and WO_3 , which was prepared by mixing and grinding 0.1 g ZFO NPs and 0.9 g WO_3 NWBs in a mortar for 30 min. The photocatalytic activity of the prepared mixture was then compared to that of ZFO, WO_3 and 10/90 ZFO/ WO_3 heterojunction, as shown in Fig. S3. The simple mixture exhibited relatively higher photocatalytic activity in evolving CO_2 than the bare ZFO and WO_3 . However, its photocatalytic activity was less than 30%, comparing with that of 10/90 ZFO/ WO_3 heterojunction. Obtained result clearly indicates that suitable heterojunction structure cannot be obtained by simply mixing two components and the charge transport between two semiconductors play a key role for the photocatalytic reactions.

In addition, monochromatic 530 nm LED lamp was applied as light source in evaluating photocatalytic activity of WO_3 NWB, ZFO NP, and 10/90 ZFO/ WO_3 samples. As shown in Fig. S4, catalytic activity of bare WO_3 was negligible in evolving CO_2 , suggesting that WO_3 with bandgap

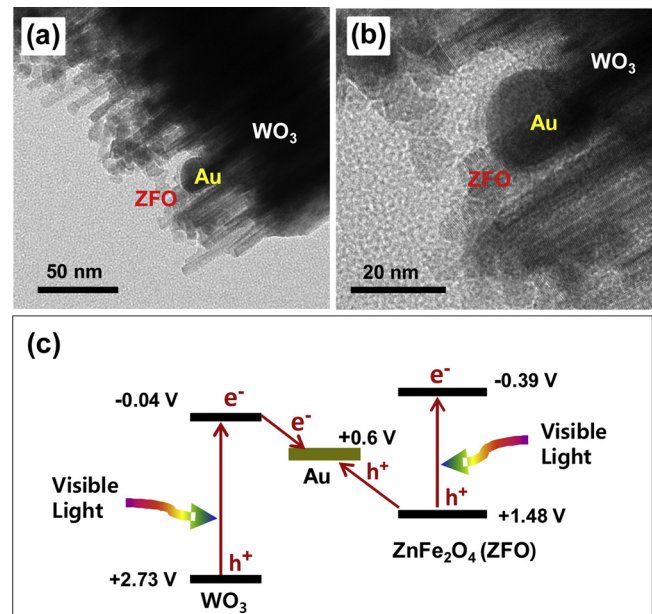


Fig. 9. TEM images of ZFO/Au/ WO_3 (a, b) and charge flow diagram during visible-light irradiation (c). All potentials were indicated vs. NHE at pH 7.

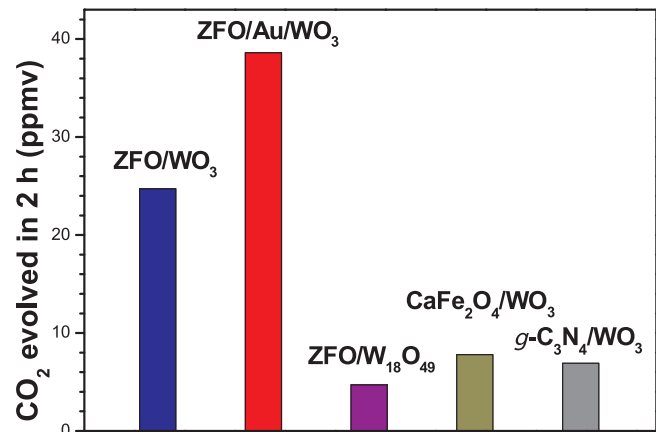


Fig. 10. Amounts of CO_2 evolved in 2 h produced by decomposition of gaseous IPA under visible-light ($\lambda \geq 422 \text{ nm}$) for various Z-scheme photocatalytic systems.

of 2.77 eV could not be excited by the photons of 530 nm. However, bare ZFO showed some activity (2.6 ppmv CO_2 in 2 h), whereas 10/90 ZFO/ WO_3 exhibited rather lower activity. No synergistic effect was found for the ZFO/ WO_3 heterojunction, suggesting that both semiconductors

must be excited by the irradiated light in order to induce inter-semiconductor charge transport.

The photocatalytic activity of ZFO/WO₃ was also compared with that of other typical Z-scheme photocatalytic systems, that is, ZFO/W₁₈O₄₉, CaFe₂O₄/WO₃, and g-C₃N₄/WO₃, as shown in Fig. 10. The W₁₈O₄₉ NWBs as-prepared by solvothermal reaction (see TEM image in Fig. 3a and b) were employed for the formation of ZFO/W₁₈O₄₉ composites. Photocatalytic activities of ZFO/W₁₈O₄₉ with various compositions were evaluated by monitoring CO₂ evolution, as shown in Fig. S5. 15/85 ZFO/W₁₈O₄₉, determined to be the optimized composition, generated only 4.5 ppm of CO₂ in 2 h, which is only 18% obtained by 10/90 ZFO/WO₃ composite. It is deduced that rapid charge recombination in W₁₈O₄₉ prevents electron transport from its CB to the VB of ZFO although W₁₈O₄₉ absorbs much more visible-light than WO₃.

The preparation procedures and TEM images of CaFe₂O₄/WO₃ and g-C₃N₄/WO₃ are shown in Fig. S6 and S7, respectively. We also found that 10/90 ZFO/WO₃ composite produced much more CO₂ in 2 h than 10/90 CaFe₂O₄/WO₃ (7.8 ppmv) and 50/50 g-C₃N₄/WO₃ (6.9 ppmv), as seen in Fig. 10. Comparing with CaFe₂O₄, ZFO absorbs more photons in the visible region. In addition, its particle size (~9 nm), which is much smaller than that of CaFe₂O₄ (~200 nm, Fig. S6) prepared by a typical method [70], is highly advantageous for the formation of effective heterojunction systems. Morphologically, we believe that tiny ZFO NPs and highly porous WO₃ NWBs are an excellent combination to make intimate contact. Particularly, in the ZFO/WO₃ system, photo-generated holes in the VB of ZFO can be scavenged efficiently by electrons in the CB of WO₃ because only a short distance migration is required for the holes in ZFO.

Comparing with g-C₃N₄, ZFO shows much higher absorption coefficient in the visible region. Moreover, ZFO is better at adsorbing organic compounds, which is one of the essential requirements for high catalytic performance.

Furthermore, ZFO/WO₃ system, composed of highly stable semiconductors, exhibits excellent chemical stability, as shown in Fig. S8. A 10/90 ZFO/WO₃ sample was repeatedly used for the photocatalytic reaction evolving CO₂ from gaseous IPA, but its activity was not appreciably decreased after 7 cycles. Consequently, ZFO/WO₃ systems with high visible-light photocatalytic activity and extended stability are regarded to be a promising candidate for commercial application. More attention is necessary to this catalytic system.

4. Conclusions

About 9 nm-sized ZFO NP with a profound visible-light absorption (E_g = 1.87 eV) was combined to highly porous WO₃ NWB with band gap of 2.77 eV to form a novel ZFO/WO₃ composites, which exhibit remarkably high visible-light photocatalytic activity by Z-scheme mechanism. Of the various compositions examined, 10:90 ZFO/WO₃ showed the highest efficiency, which is attributed to the balanced light absorption by ZFO and WO₃. That is, the irradiated light can be utilized effectively and the charge recombination in the Z-scheme ZFO/WO₃ system can be minimized, when equal amounts of charges are generated from ZFO and WO₃. Remarkably, the catalytic efficiency of 10:90 ZFO/WO₃ was ~3.0 times that of N-TiO₂ with respect to the evolution of CO₂ from gaseous IPA and ~7 times that of N-TiO₂ in decomposing aqueous SA, mainly caused by the formation of both •OH and •O₂⁻ species. Moreover, coupling of sub 10 nm ZFO NPs and highly porous WO₃ NWBs is regarded to be an outstanding combination. Morphologically, an intimate contact can be achieved between ZFO and WO₃, and the photo-generated holes in the ZFO VB can be scavenged efficiently by the electrons in the WO₃ CB because the holes in ZFO migrate only a short distance.

Declaration of Competing Interest

The authors declare no competing financial interests.

Acknowledgments

This work was supported by the National Research Foundation of Korea (NRF) (NRF-2018R1A2B6004766 and NRF-2015R1D1A1A01057390) and the Korea Center for Artificial Photosynthesis (KCAP) funded by the Ministry of Science and ICT through the National Research Foundation of Korea (No. 2016M1A2A2947946).

Appendix A. Supplementary data

Supplementary material related to this article can be found, in the online version, at doi:<https://doi.org/10.1016/j.apcatb.2019.117856>.

References

- [1] T. Inoue, A. Fujishima, S. Konishi, K. Honda, *Nature* 277 (1979) 637–638.
- [2] M.R. Hoffmann, S.T. Martin, W. Choi, D.W. Bahnemann, *Chem. Rev.* 95 (1995) 69–96.
- [3] A. Kubacka, M. Fernandez-Garcia, G. Colon, *Chem. Rev.* 112 (2012) 1555–1614.
- [4] A.L. Linsebigler, G. Lu, J.T. Yates, *Chem. Rev.* 95 (1995) 735–758.
- [5] M. Grätzel, *Nature* 414 (2001) 338–344.
- [6] N. Serpone, P. Maruthamuthu, P. Pichat, E. Pelizzetti, H. Hidaka, *J. Photochem. Photobiol.*, A 85 (1995) 247–255.
- [7] M. Anpo, M. Takeuchi, *J. Catal.* 216 (2003) 505–516.
- [8] X. Qiu, M. Miyachi, K. Sunada, M. Minoshima, M. Liu, Y. Lu, D. Li, Y. Shimodaira, Y. Hosogi, Y. Kuroda, K. Hashimoto, *ACS Nano* 6 (2012) 1609–1618.
- [9] V. Stengl, V. Houskova, S. Bakardjieva, N. Murafa, *ACS Appl. Mater. Interfaces* 2 (2010) 575–580.
- [10] E. Borgarello, J. Kiwi, M. Grätzel, E. Pelizzetti, M. Visca, *J. Am. Chem. Soc.* 104 (1982) 2996–3002.
- [11] H. Yamashita, M. Harada, J. Misaka, M. Takeuchi, K. Ikeue, M. Anpo, *J. Photochem. Photobiol.*, A 148 (2002) 257–261.
- [12] P. Bouras, E. Stathatos, P. Lianos, *Appl. Catal. B* 73 (2007) 51–59.
- [13] R. Asahi, T. Morikawa, T. Ohwaki, K. Aoki, Y. Taga, *Science* 293 (2001) 269–271.
- [14] S.-I. In, A.H. Kean, A. Orlov, M.S. Tikhov, R.M. Lambert, *Energy Environ. Sci.* 2 (2009) 1277–1279.
- [15] J.C. Yu, W. Ho, J. Yu, H. Yip, P.K. Wong, J. Zhao, *Environ. Sci. Technol.* 39 (2005) 1175–1179.
- [16] J. Zhu, F. Fan, R. Chen, H. An, Z. Feng, C. Li, *Angew. Chem. Int. Ed.* 54 (2015) 9111–9114.
- [17] T. Tachikawa, T. Ochi, Y. Kobori, *ACS Catal.* 6 (2016) 2250–2256.
- [18] Y. Hu, D. Li, Y. Zheng, W. Chen, Y. He, Y. Shao, X. Fu, G. Xiao, *Appl. Catal. B* 104 (2011) 30–36.
- [19] J. Wu, F. Duan, Y. Zheng, Y. Xie, *J. Phys. Chem. C* 111 (2007) 12866–12871.
- [20] Z. Yi, J. Ye, N. Kikugawa, T. Kako, S. Ouyang, H.S. Williams, H. Yang, J. Cao, W. Luo, Z. Li, Y. Liu, R.L. Withers, *Nat. Mater.* 9 (2010) 559–564.
- [21] S.B. Rawal, S.D. Sung, W.I. Lee, *Catal. Commun.* 17 (2012) 131–135.
- [22] J. Ma, J. Zou, L. Li, C. Yao, T. Zhang, D. Li, *Appl. Catal. B* 134–135 (2013) 1–6.
- [23] Y. Liu, H. Yu, M. Cai, J. Sun, *Catal. Commun.* 26 (2012) 63–67.
- [24] F. Ji, C. Li, J. Zhang, *ACS Appl. Mater. Interfaces* 2 (2010) 1674–1678.
- [25] H.G. Kim, P.H. Borse, J.S. Jang, E.D. Jeong, J.S. Lee, *Mater. Lett.* 62 (2008) 1427–1430.
- [26] X. Zhang, Z. Ai, F. Jia, L. Zhang, *J. Phys. Chem. C* 112 (2008) 747–753.
- [27] Y. Lei, G. Wang, S. Song, W. Fan, M. Pang, J. Tang, H. Zhang, *Dalton Trans.* 39 (2010) 3273–3278.
- [28] J. Low, J. Yu, M. Jaroniec, S. Wageh, A.A. Al-Ghamdi, *Adv. Mater.* 29 (2017) 1601694.
- [29] H. Li, Y. Zhou, W. Tu, J. Ye, Z. Zou, *Adv. Funct. Mater.* 25 (2015) 998–1013.
- [30] W. Liao, M. Muruganathan, Y. Zhang, *Phys. Chem. Chem. Phys.* 17 (2015) 8877–8884.
- [31] J. Zhang, Y. Hu, X. Jiang, S. Chen, S. Meng, X. Fu, *J. Hazard. Mater.* 280 (2014) 713–722.
- [32] S.B. Rawal, S. Bera, D. Lee, D.J. Jang, W.I. Lee, *Catal. Sci. Technol.* 3 (2013) 1822–1830.
- [33] S. Bera, S.B. Rawal, H.J. Kim, W.I. Lee, *ACS Appl. Mater. Interfaces* 6 (2014) 9654–9663.
- [34] T. Arai, M. Yanagida, Y. Konishi, Y. Iwasaki, H. Sugihara, K. Sayama, *J. Phys. Chem. C* 111 (2007) 7574–7577.
- [35] S. Chen, L. Ji, W. Tang, X. Fu, *Dalton Trans.* 42 (2013) 10759–10768.
- [36] Z. Liu, Z.-G. Zhao, M. Miyachi, *J. Phys. Chem. C* 113 (2009) 17132–17137.
- [37] H.G. Kim, E.D. Jeong, P.H. Borse, S. Jeon, K. Yong, J.S. Lee, W. Li, S.H. Oh, *Appl. Phys. Lett.* 89 (2006) 064103.
- [38] K. Katsumata, R. Motoyoshi, N. Matsushita, K. Okada, *J. Hazard. Mater.* 260 (2013) 475–482.
- [39] S. Chen, Y. Hu, S. Meng, X. Fu, *Appl. Catal. B* 150–151 (2014) 564–573.
- [40] H. Katsumata, T. Hayashi, M. Taniguchi, T. Suzuki, S. Kaneko, *Mater. Sci. Semicond. Process* 25 (2014) 68–75.
- [41] Z. Chen, W. Wang, Z. Zhang, X. Fang, *J. Phys. Chem. C* 117 (2013) 19346–19352.
- [42] N. Tian, H. Huang, Y. He, Y. Guo, T. Zhang, Y. Zhang, *Dalton Trans.* 44 (2015) 4297–4307.

[43] X. Chen, X. Huang, Z. Yi, *Chem. Eur. J.* 20 (2014) 17590–17596.

[44] X. Wang, M. Hong, F. Zhang, Z. Zhuang, Y. Yu, *ACS Sustainable Chem. Eng.* 4 (2016) 4055–4063.

[45] R. Bhosale, S. Jain, C.P. Vinod, S. Kumar, S. Ogale, *ACS Appl. Mater. Interfaces* 11 (2019) 6174–6183.

[46] Z. Li, X. Meng, Z. Zhang, *Catal. Today* 315 (2018) 67–78.

[47] F. Chen, C. Wu, J. Wang, C.P. Francois-Xavier, T. Wintgens, *Appl. Catal. B* 250 (2019) 31–41.

[48] S.H. Xu, D.L. Feng, W.F. Shangguan, *J. Phys. Chem. C* 113 (2009) 2463–2467.

[49] X. Zhu, F. Zhang, M. Wang, J. Ding, S. Sun, J. Bao, C. Gao, *Appl. Surf. Sci.* 319 (2014) 83–89.

[50] X. Guo, H. Zhu, Q. Li, *Appl. Catal. B* 160–161 (2014) 408–414.

[51] Y. Huang, D. Zhu, Q. Zhang, Y. Zhang, J.J. Gao, Z. Shen, W. Ho, S.C. Lee, *Appl. Catal., B* 234 (2018) 70–78.

[52] G. Hou, Y. Zhang, S. Gao, *Mater. Lett.* 209 (2017) 598–601.

[53] C.-H. Chen, Y.-H. Liang, W.-D. Zhang, *J. Alloys Compd.* 501 (2010) 168–172.

[54] Y.T. Kwon, K.Y. Song, W.I. Lee, G.J. Choi, Y.R. Do, *J. Catal.* 191 (2000) 192–199.

[55] J.G. Chen, C.Y. Chen, C.G. Wu, C.Y. Lin, Y.H. Lai, C.C. Wang, H.W. Chen, R. Vittal, K.C. Ho, *J. Mater. Chem.* 20 (2010) 7201–7207.

[56] F. Fabregat-Santiago, G. Garcia-Belmonte, J. Bisquert, P. Bogdanoff, A. Zaban, *J. Electrochem. Soc.* 150 (2003) 293–298.

[57] X. Li, Y. Hou, Q. Zhao, G. Chen, *Langmuir* 27 (2011) 3113–3120.

[58] Y. Hou, X.Y. Li, Q.D. Zhao, X. Quan, G.H. Chen, *Adv. Funct. Mater.* 20 (2010) 2165–2174.

[59] G.G. Liu, X.Z. Zhang, Y.J. Xu, X.S. Niu, L.Q. Zheng, X.J. Ding, *Chemosphere* 55 (2013) 1287–1291.

[60] S.B. Rawal, H.J. Kim, W.I. Lee, *Appl. Catal. B* 142–143 (2013) 458–464.

[61] P.R. Harvey, R. Rudham, S. Ward, *J. Chem. Soc., Faraday Trans.* 79 (1983) 1381–1390.

[62] Y. Ohko, K. Hashimoto, A. Fujishima, *J. Phys. Chem. A* 101 (1997) 8057–8062.

[63] Y. Nosaka, Y. Yamashita, H. Fukuyama, *J. Phys. Chem. B* 101 (1997) 5822–5827.

[64] D. Chatterjee, A. Mahata, *J. Photochem. Photobiol., A* 165 (2004) 19–23.

[65] S. Ding, J. Niu, Y. Bao, L. Hu, *J. Hazard. Mater.* 262 (2013) 812–818.

[66] W.J. Li, D.Z. Li, Y.M. Lin, P.X. Wang, W. Chen, X.Z. Fu, Y. Shao, *J. Phys. Chem. C* 116 (2012) 3552–3560.

[67] W.J. Wang, L.Z. Zhang, T.C. An, G.Y. Li, H.Y. Yip, P.K. Wong, *Appl. Catal. B* 108–109 (2011) 108–116.

[68] L. Ye, J. Liu, C. Gong, L. Tian, T. Peng, L. Zan, *ACS Catal.* 2 (2012) 1677–1683.

[69] Z. Chen, F. Bing, Q. Liu, Z. Zhang, X. Fang, *J. Mater. Chem. A* 3 (2015) 4652–4658.

[70] R.A. Candeia, M.I.B. Bernardi, E. Longo, I.M.G. Santos, A.G. Souza, *Mater. Lett.* 58 (2004) 569–572.